processes

MDPI

Article

Effects of a Detached Eddy Simulation-Curvature Correction (DES-CC) Turbulence Model on the Unsteady Flows of Side Channel Pumps

Runshi Liu [1], Fan Zhang [1,*], Ke Chen [1], Yefang Wang [1], Shouqi Yuan [1] and Ruihong Xu [2]

[1] National Research Center of Pumps, Jiangsu University, Zhenjiang 212013, China
[2] Kunming Electrical Machinery Company Limited, Kunming 650100, China
* Correspondence: fzhang@ujs.edu.cn

Abstract: A side channel pump is a pump with a high head and a small flow that is widely used in various industrial fields. Many scientists have studied the hydraulic performance, pressure fluctuation characteristics, and gas-liquid mixed transport characteristics of this type of pump. However, these studies mainly focused on the single-stage impeller of the side channel pump, without considering the inter-stage connection channel and the multistage timing effect. These characteristics affect the hydraulic performance and pressure-pulsation characteristics of the side channel pump. Therefore, we carried out a numerical simulation and an experimental comparison on the multistage side channel pump to explore its flow characteristics during the stages. This study focused on the influence of different turbulence models on the numerical simulation of multistage side channel pumps. Shear stress transport (SST), detached eddy simulation (DES), and detached eddy simulation-curvature correction (DES-CC) turbulence models were selected for consideration. By studying the pressure and velocity streamline distribution, the turbulent kinetic energy, and the shape and volume of the vortex core area simulated by the three models, we concluded that the DES-CC model, when compared to the other models, can more fully reflect the vortex characteristics and the simulation results that are closer to the experimental data. The results of this study can be used as the basis for future research on multistage side channel pumps.

Keywords: side channel pump; turbulence modeling; detached eddy simulation (DES); curvature correction (CC); vortex

Citation: Liu, R.; Zhang, F.; Chen, K.; Wang, Y.; Yuan, S.; Xu, R. Effects of a Detached Eddy Simulation-Curvature Correction (DES-CC) Turbulence Model on the Unsteady Flows of Side Channel Pumps. *Processes* **2022**, *10*, 1630. https://doi.org/10.3390/pr10081630

Academic Editor: Václav Uruba

Received: 2 August 2022
Accepted: 15 August 2022
Published: 17 August 2022

1. Introduction

A side channel pump is a type of vortex pump that, when compared with other common vane pumps, has the advantages of a small flow rate, a strong single-stage pressure boosting capability, self-priming, and mixed gas–liquid transportation. Because of their advantages, side channel pumps are widely used in the petrochemical, aerospace, shipbuilding, automotive, mining, and other industries. However, due to their complex internal flow behavior, side channel pumps exhibit many unique vortices, leading to low efficiency and adverse effects, such as noise, vibration, and channel blockage [1].

Research on side channel pumps can be traced back to the early 20th century. The main research was focused on the performance optimization of single-stage side channel pumps. Shirinov and Oberbeck [2–4] proposed four different vane shapes (C, V, T, and Y) and obtained their performance differences experimentally. They found that the compression ratio of a side channel pump depends on the number of blades at the periphery of the impeller. When the impeller diameter increases or the size of the side channel decreases, then the optimal number of blades increases. Later, Fleder and Böhle [5,6] conducted a series of investigations on the effect of blade length, blade width, and side channel height on the performance of side channel pumps. They found that the performance of side channel pumps is mainly affected by the ratio of blade height to the radius and the ratio

of side channel height to blade radius, while the ratio of side channel height to blade height is uniform. Recently, Zhang [7–9] et al. analyzed the effects of the blade angle and the side channel wrapping angle on the side channel pump, using various methods, including entropy production analysis. They found that these parameters have significant effects on the hydraulic performance and pressure pulsation of the side channel pump. In addition, they investigated the transient flow characteristics at different blade suction angle profiles and found that the pressure fluctuation and frequency of the side channel pump were related to the flow exchange between the impeller and the side channel. In addition, they [10–12] optimized the side channel pump by adding a convex blade and found that the convex vanes can expand the high efficiency area of the side channel pump.

Recently, hybrid Reynolds-averaged Navier–Stokes (RANS) and large eddy simulation (LES) models have been widely used in numerical simulations [13–15]. Due to the advantages of the $k-\varepsilon$ and the $k-\omega$ models, the shear stress transport (SST) model is the most widely used RANS model [16]. However, the RANS model is not accurate for some numerical simulations because it overestimates eddy viscosity and ignores some small-scale vortices. Large eddy simulation (LES) can solve the simulation problem of small-scale eddy currents, but overestimates the wall vortex; thus, a wall correction model is required [17]. At the same time, the computing resource demands of the LES model are higher than those of the RANS model. To integrate the advantages of both models, many RANS–LES hybrid models have been proposed. The detached eddy simulation (DES) model of Spalart [18] is one of the most famous hybrid models. It replaces the area where the eddy current characteristic length predicted by the RANS model is greater than the grid element size with the LES model for numerical simulations.

The above studies focused on the performance and internal flow theory of single-stage side channel impellers, with a lack of relevant research on the hydraulic performance, pressure pulsation, and timing effect of multistage side channel pumps. Therefore, we carried out numerical and experimental comparisons for multistage side channel pump under a detached eddy simulation-curvature correction (DES-CC) model. This study can serve as a foundation for future investigations into the characteristics of multistage side channel pumps and other low specific speed pumps.

2. Turbulence Modeling

The classification of existing turbulence numerical simulation methods is based on the comprehensiveness of an energy spectrum analysis of turbulence fluctuation. There are three basic methods: direct numerical simulation (DNS), LES, and RANS.

The DNS method can theoretically obtain the most accurate simulation results, but it requires Kolmogorov micro-scale numerical resolution in space and time. It also requires huge computational resources and provides excessive simulation information, which makes it almost impossible for use in engineering.

The RANS model is based on a Reynolds-averaged Navier–Stokes equation. By decomposing the instantaneous velocity value into the sum of the average value and the fluctuation component, the Reynolds equation is derived. The equation describes the turbulence by decomposing the velocity U_i into average velocity $\overline{U_i}$ and wave velocity u_i. In fact, the transport equations of turbulent stress can be derived from the initial and the average Navier–Stokes equations. However, the derived relation still has an unknown high-order correlation, so other equations must be introduced to close the equations.

The RANS model is divided into a zero-equation model, two-equation turbulence models, and one equation model by the difference in the number of equations of the closed system equations. The zero-equation model is only suitable for relatively simple flows. The one-equation model is highly specialized, while the two-equation model is widely used. Typically, the two-equation models are the $k-\varepsilon$ and the $k-\omega$ models. They use the gradient diffusion assumption to correlate Reynold stress with turbulent viscosity, which is the product of turbulent velocity and turbulent length scale. The turbulent velocity is given by the turbulent kinetic energy, and the turbulent length scale is the difference

between the two models. The $k-\varepsilon$ model is used to solve the turbulent kinetic energy k and the turbulent dissipation rate ε; the $k-\omega$ model is used to solve the turbulent kinetic energy k and the turbulent frequency ω. The $k-\varepsilon$ model has the advantage of better vortex simulation for the separated surface, but it has the disadvantage of poor treatment for wall-flow. The $k-\omega$ model can accurately handle wall-flow, but its requirements for inlet and outlet conditions are more stringent. A small disturbance will have a great impact on the simulation results of the $k-\omega$ model.

The SST model, which is a type of RANS model, is a turbulence model that is commonly used in hydraulic machinery numerical simulations. To solve the high dependence of the $k-\omega$ model on inlet and outlet conditions, the $k-\varepsilon$ model and the $k-\omega$ model are mixed. The SST model requires that the two turbulence models deal with the wall region and the central region, respectively, by adjusting the parameters F_1 and F_2. In this way, it combines the advantages of the $k-\varepsilon$ model and the $k-\omega$ model, reduces the serious dependence on import and export conditions, and retains good accuracy and robustness. The relations of the model are as follows [19].

$$\frac{\partial(\rho k)}{\partial t}+\frac{\partial}{\partial x_j}(\rho U_j k)=\frac{\partial}{\partial x_j}\left[\left(\mu+\frac{\mu_t}{\sigma_k}\right)\frac{\partial k}{\partial x_j}\right]+P_k-\beta'\rho k\omega \tag{1}$$

$$\begin{array}{l}\frac{\partial(\rho\omega)}{\partial t}+\frac{\partial}{\partial x_j}(\rho U_j\omega)=\\ \frac{\partial}{\partial x_j}\left[\left(\mu+\frac{\mu_t}{\sigma_{\omega 3}}\right)\frac{\partial\omega}{\partial x_j}\right]+(1-F_1)2\rho\frac{1}{\sigma_{\omega 2}2\omega}\frac{\partial k}{\partial x_j}\frac{\partial\omega}{\partial x_j}+\alpha\frac{\omega}{k}P_k-\beta_3\rho\omega^2\end{array} \tag{2}$$

with

$$\frac{\mu_t}{\rho}=\frac{a_1 k}{\max(a_1\omega, SF_2)} \tag{3}$$

$$F_1=\tanh\left(\arg_1^4\right) \tag{4}$$

$$\arg_1=\min\left(\max\left(\frac{\sqrt{k}}{\beta'\omega y},\frac{500v}{y^2\omega}\right),\frac{4\rho k}{CD_{k\omega}\sigma_{e2}y^2}\right) \tag{5}$$

$$CD_{k\omega}=\max\left(2\rho\frac{1}{\sigma_{\omega 2}\omega}\frac{\partial k}{\partial x_j}\frac{\partial\omega}{\partial x_j},1.0\times10^{-10}\right) \tag{6}$$

$$F_2=\tanh\left(\arg_2^2\right),\arg_2=\max\left(\frac{2\sqrt{k}}{\beta'\omega y},\frac{500v}{y^2\omega}\right) \tag{7}$$

$$\Phi_3=(1-F_1)\Phi_2+\Phi_1 \tag{8}$$

The above model will generate excessive turbulent energy near the stagnation point, so it is strictly limited. Nevertheless, the development of engineering technology has resulted in higher requirements for numerical simulation. To solve the separation of vortices that are larger than the grid element scale and vortices that are smaller than the grid element scale, and to obtain more accurate vortex details, the LES model is required. The LES model can calculate pressure scale vortices by modifying some parameters. One of the key formulae of the LES model is the filtering formula [20].

$$\overline{\Phi}(x)=\int_D \Phi(x')G(x;x')dx \tag{9}$$

with

$$G(x;x')=\begin{cases}1/V, x'\in V\\ 0 \text{ otherwise}\end{cases} \tag{10}$$

where $G(x,x')$ is the filter function.

After applying the filtering formula, the N–S equation can be written in the following format [20].

$$\frac{\partial}{\partial t}\left(\overline{\rho}\overline{U}_i\right)+\frac{\partial}{\partial x_j}\left(\overline{\rho}_{U_j}\right)=-\frac{\partial \overline{p}}{\partial x_i}+\frac{\partial}{\partial x_j}\left[\mu\left(\frac{\partial \overline{U}_i}{\partial x_j}+\frac{\partial \overline{U}_j}{\partial x_i}\right)\right]+\frac{\partial \tau_{ij}}{\partial x_j} \tag{11}$$

with

$$\tau_{ij}=-\overline{\rho U_i U_j}+\overline{\rho}\,\overline{U_i}\,\overline{U_j} \tag{12}$$

The relationship between the sub-grid-scale stress τ_{ij} and the large-scale strain rate tensor $\overline{S_{ij}}$ [20] is as follows:

$$\tau_{ij}-\frac{1}{3}\delta_{ij}\tau_{kk}=2\mu_{sgs}\overline{S_{ij}} \tag{13}$$

$$\overline{S_{ij}}=\frac{1}{2}\left(\frac{\partial \overline{U_i}}{\partial x_j}+\frac{\partial \overline{U_j}}{\partial x_i}\right) \tag{14}$$

However, the use of the LES model in the near-wall region consumes too many resources, and the excessive vortex simulation in this region must be modified. Therefore, the detached eddy simulation (DES) model is proposed. The DES model is attempts to combine the elements of the RANS and LES formulae to obtain a hybrid formula, in which the RANS model is used in an additional and mildly separated boundary layer. In the simulation of the DES model, when the turbulence length L_t, predicted by the RANS model, is greater than the local grid spacing, it is converted from the RANS model to the LES model. At this time, the length scale of the dissipation rate Δ that is used in the calculation of the turbulent kinetic energy equation is replaced by the local grid spacing [20]:

$$\frac{\partial(\rho k)}{\partial t}+\frac{\partial}{\partial x_j}(\rho U_j k)=\frac{\partial}{\partial x_j}\left[\left(\mu+\frac{\mu_t}{\sigma_{k3}}\right)\frac{\partial k}{\partial x_j}\right]+P_k-\beta'\rho k\omega F_{DES} \tag{15}$$

$$F_{DES}=\max\left(\frac{L_t}{C_{DES}\Delta},1\right) \tag{16}$$

$$\Delta=\max(\Delta_i) \tag{17}$$

$$L_t=(\sqrt{k})/\beta'\omega \tag{18}$$

All of the above turbulence models adopt the assumption of eddy viscosity, which leads to their common disadvantages; that is, they are insensitive to the flow curvature and the system rotation, which produces errors in the fluid simulation of high-speed rotation; accordingly, the equation needs to be modified. Some studies have shown that curvature correction can improve numerical simulation [21]. In this study, the equation is corrected by correcting P_k. The relevant formulae are as follows [22]:

$$P_k \rightarrow P_k \cdot f_r \tag{19}$$

$$f_r=\max\left[0,1+C_{\text{scale}}\left(\widetilde{f}_r-1\right)\right] \tag{20}$$

$$\widetilde{f}_r=\max\{\min(f_{\text{rotation}},1.25),0\} \tag{21}$$

$$f_{\text{rotation}}=(1+c_{r1})\frac{2r^*}{1+r^*}\left[1-c_{r3}\tan^{-1}(c_{r2}\widetilde{r})\right]-c_{r1} \tag{22}$$

It can be seen that the turbulence model has an impact on the results of the numerical simulation. However, no one has carried out an analysis of the simulation results under different mathematical models of multistage side channel pumps. In this paper, the effects of the RANS–LES hybrid model and curvature correction on the numerical simulation of multistage side channel pumps are compared and analyzed, and the corresponding conclusions are provided.

3. Numerical Model and Simulation

3.1. The Pump Model and Mesh

The pump model used in this study is a three-stage side channel pump comprising a one-stage front centrifugal impeller and a two-stage side channel impeller. Table 1 shows the geometric dimensions of the key components of the pump. The rotational speed and the flow rate of the pump are 2900 r/min and 7.95 m^3/h, respectively. As shown in Figure 1, the structure of the pump is very complex. The pump's flow body is divided into seven domains, as follows: inlet passage, centrifugal impeller, centrifugal impeller outlet passage, side channel impeller front passage, side channel impeller, side channel impeller inlet, and outlet passages. In this model pump, the two-stage side channel impeller and its attached channel are consistent in geometry, except that there is an included angle of 180 degrees in the circumferential arrangement of the two sections. This challenges the mesh generation of the structured grids and reduces the calculation accuracy of the structured grids.

Table 1. Geometric specifications of key components of the multistage side channel pump.

Geometrical Parameters	Symbol (Unit)	Value
Inlet inner diameter	D_1 (mm)	40.0
Outlet inner diameter	D_2 (mm)	32.0
Number of centrifugal impeller blades	Z_1	6
Outer diameter of centrifugal impeller	D_3 (mm)	120
Inlet diameter of centrifugal impeller	D_4 (mm)	40.0
Number of impeller blades in side channel	Z_2	24
Blade width of side channel impeller	w (mm)	10.0
Blade thickness of side channel impeller	b (mm)	5.40
Outer diameter of side channel impeller	D_5 (mm)	130

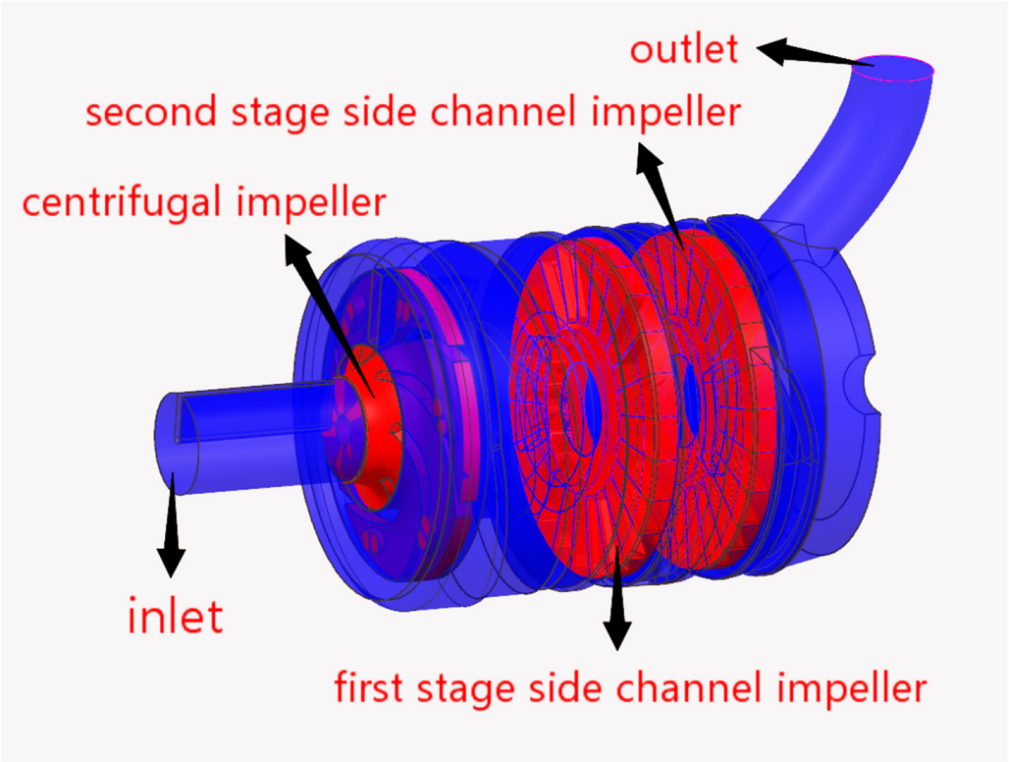

Figure 1. Water structure diagram of the investigated multistage side channel pump.

Therefore, the centrifugal and side channel impeller flow domains, which serve as the main working components, were meshed with structured grids, whereas the other flow domains of the other components were meshed with unstructured grids. The structured grids of the centrifugal impeller and the side channel impeller are shown in Figure 2.

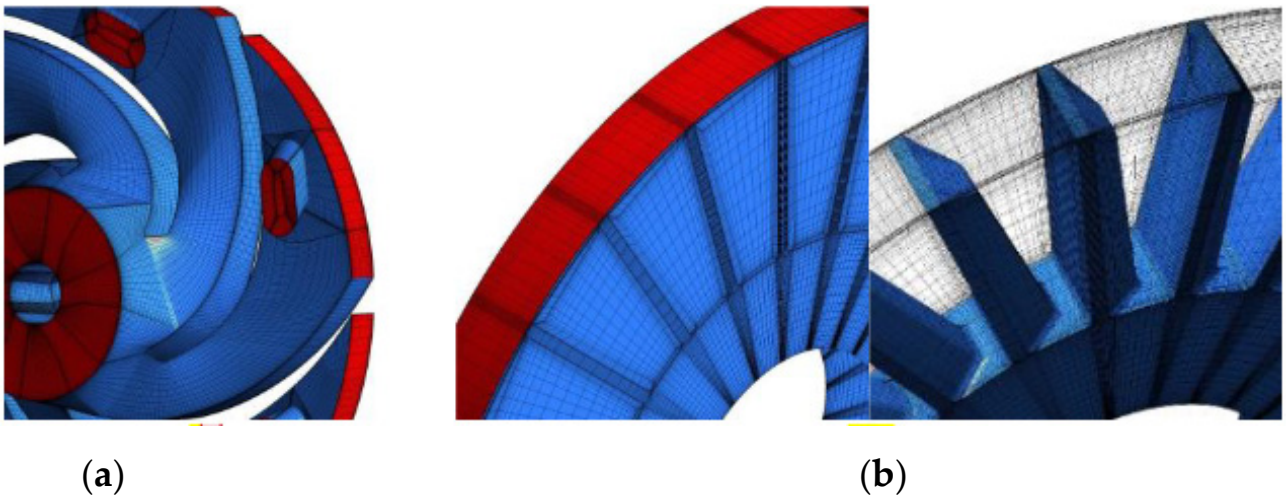

Figure 2. Partial mesh view of the flow domain: (**a**) centrifugal impeller; (**b**) side channel impeller.

To determine the appropriate number of grids for the numerical simulations, a grid independence test was carried out based on the SST model. As shown in Figure 3, when the number of grids reached 30 million, a change in the head resulted, with a number of grids that was not obvious, but the efficiency increased steadily. At the same time, as shown in Figure 4, the Y^+ of the main flow part was basically less than 30, while most parts of the side channel pump impeller were less than 5. This met the requirements of calculation accuracy; thus, all of the simulations for the study were meshed using these methods, for consistency.

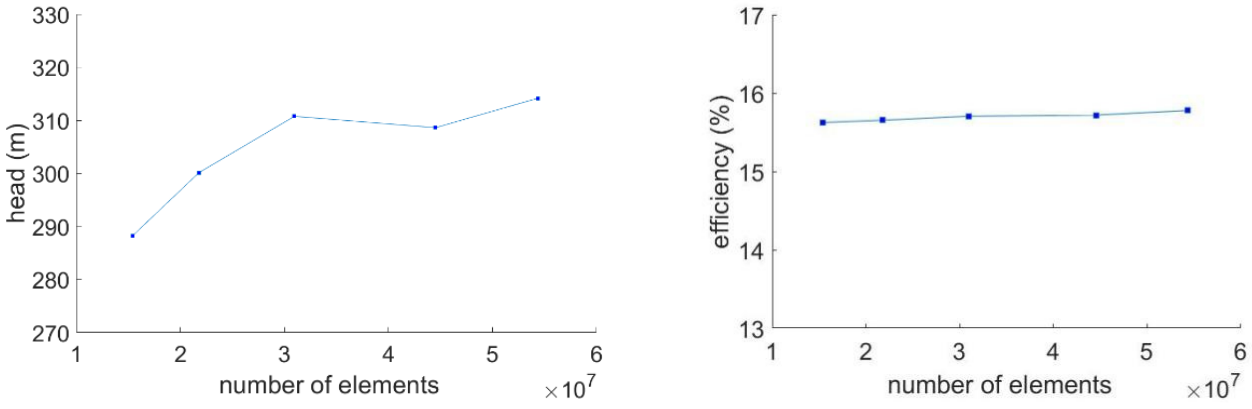

Figure 3. Grid independence verification diagram.

3.2. Boundary Conditions of Numerical Simulations

The setting parameters of the numerical simulation are shown in Table 2. In the numerical simulation, the static pressure inlet and mass flow outlet were used. The upwind scheme was selected to calculate the advection term in the discrete finite volume equation. Setting the upwind scheme had the best robustness in the CFX simulation [23]. Considering the operating conditions of the pump, the simulation was set as an isothermal model at 25 °C. The wall surface was set as a no-slip wall. Considering that all parts except the side channel impeller were cast iron, the roughness of other surfaces was set to 0.25 mm, and the roughness of the side channel impeller surface was set to 0.05 mm. For the steady state

interface, the "frozen rotor" was selected, and the "transient rotor–stator" was selected for the transient simulations. The transient time step was set to 0.000172414 s, which was the time taken for the impeller to rotate at an angle of 3 degrees. The impeller was set operate at rotational speed of 2900 r/min.

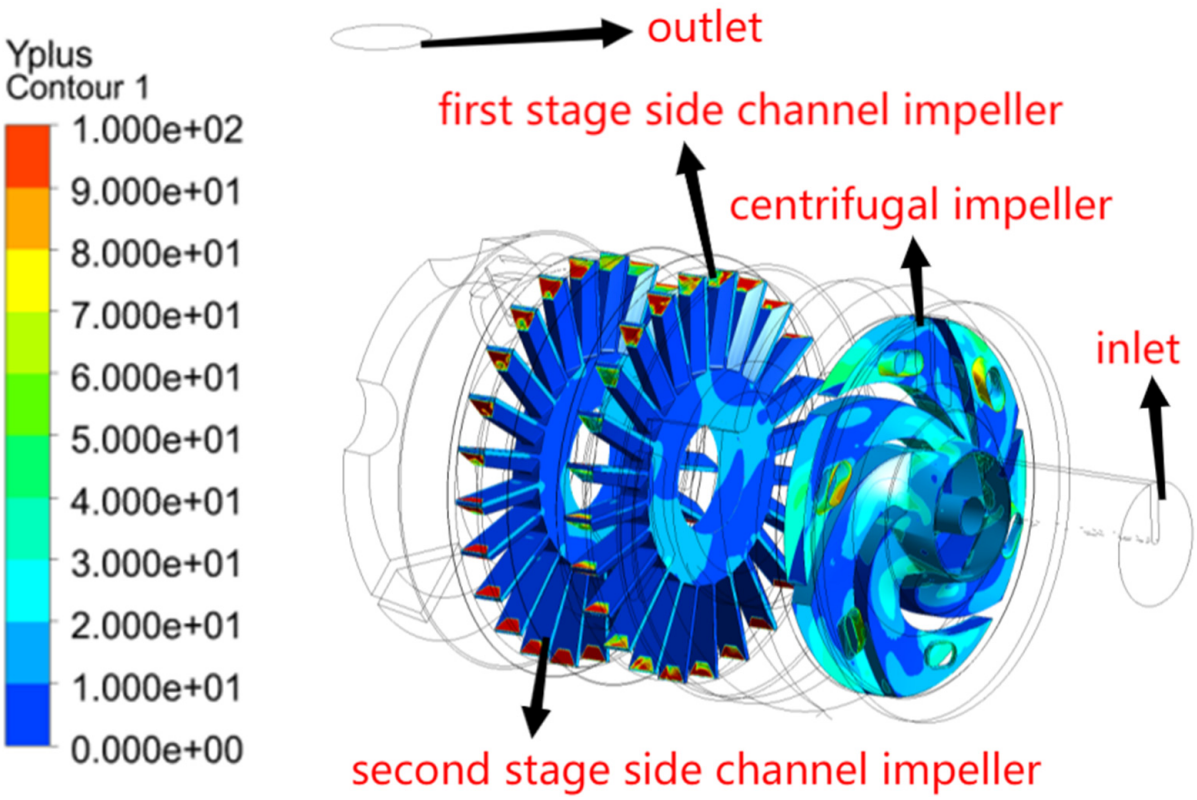

Figure 4. Schematic diagram of impeller grid Y^+.

Table 2. Setting mode of CFX.

Location	Boundary Type	Mass and Momentum
Inlet of inlet extension	Inlet	Static pressure
Outlet of outlet extension	Outlet	Mass flow rate
Physical surfaces	Wall	No-slip wall
Rotor–stator interfaces		
Steady state	Frozen rotor	
Transient state	Transient rotor–stator	
Solver control for transient simulation		
Time-step	0.000172414 s	
Maximum number of timesteps	600	
RMS residual	10^{-4}	

To compare the simulation differences between the RANS model and the RANS–LES hybrid model, the SST model and the DES model were used as the control groups. To verify the influence of curvature correction on the numerical simulation of a multistage side channel pump, the simulation results before and after the addition of curvature correction were compared, based on the DES model.

4. Results and Discussion

4.1. Comparison of the SST and DES Models

It can be seen from Figure 5 that the transient results showed regular periodic changes since the second impeller rotation, with no unstable changes. The time-averaged data of the last four cycles of the transient simulations were used to compute the hydraulic performance.

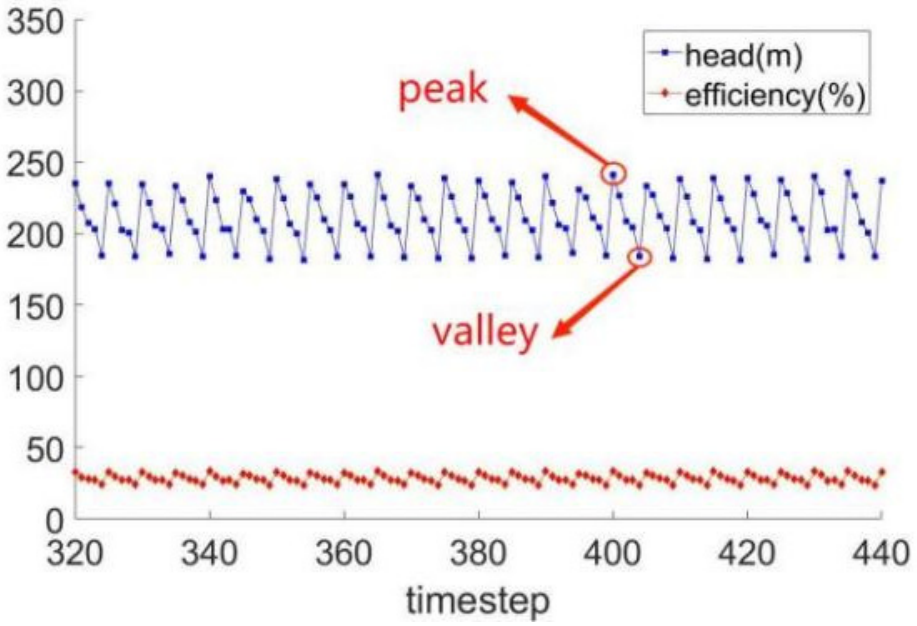

Figure 5. Schematic diagram of simulated sampling time points.

The simulated results of head and efficiency for the two turbulence models, SST and DES, at different flow points are shown in Table 3 and Figure 6. It can be seen from Figure 6 that the hydraulic performance simulation results of the SST and DES models were similar. Due to the complex internal flow behavior and the high head of the pump, the numerical simulation accuracy of the pump was low. As the flow rate increased, the head decreased and the efficiency increased gradually, in line with the working principle of the side channel pump. This showed that the simulation results reflected the internal flow characteristics of the multistage side channel pump and could be depended upon to analyze its internal flow mechanism. To identify the characteristics of a side channel pump, the peak and valley points of its head were selected as the time points for the analysis. The velocity streamlines and the pressure contour diagrams at the flow rate of 7.95 m^3/h are shown in Figure 7 It can be seen that the flow behavior of the pump was extremely complex and the velocity streamlines were chaotic. To identify the working characteristics of the multistage side channel pump, as shown in Figure 8, the mid-shaft section of A1 and A2 of the side channel impellers and the meridional section of runner A3 were selected. A1 and A2 showed the working condition of the key component (the side channel impeller), while A3 provided an overall flow performance of the model pump.

Table 3. Hydraulic performance of the SST and DES models at different flow points.

Flow Rate Q (m^3/h)	**Q = 4.00**		**Q = 7.95**		**Q = 12.02**	
Turbulence model	SST	DES	SST	DES	SST	DES
Head/(m)	310.96	314.35	211.30	211.18	105.94	108.57
Efficiency/(%)	15.688	15.727	28.390	28.440	31.925	31.918

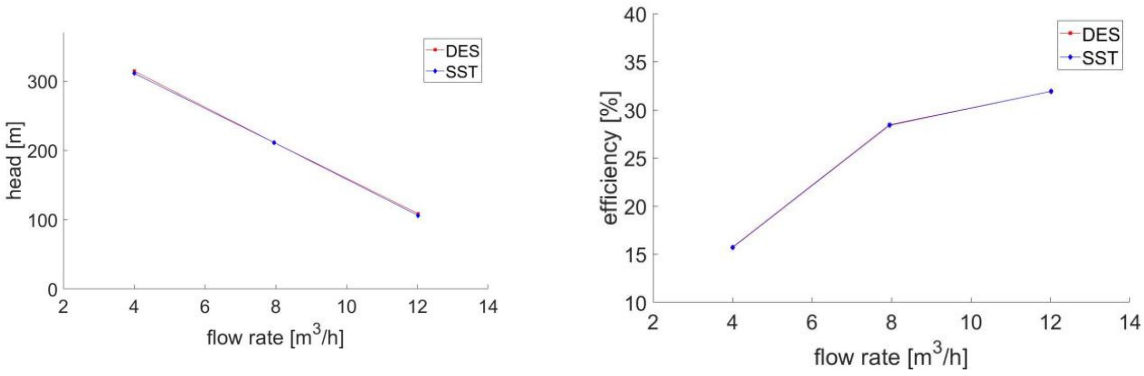

Figure 6. The hydraulic performance simulation results with the SST and DES models at different flow points.

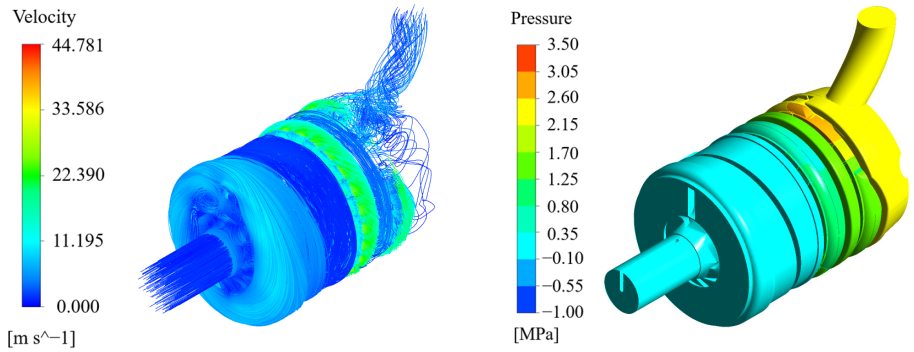

(**a**) (**b**)

Figure 7. Overall description of a multistage side channel pump: (**a**) streamline and velocity; (**b**) surface pressure.

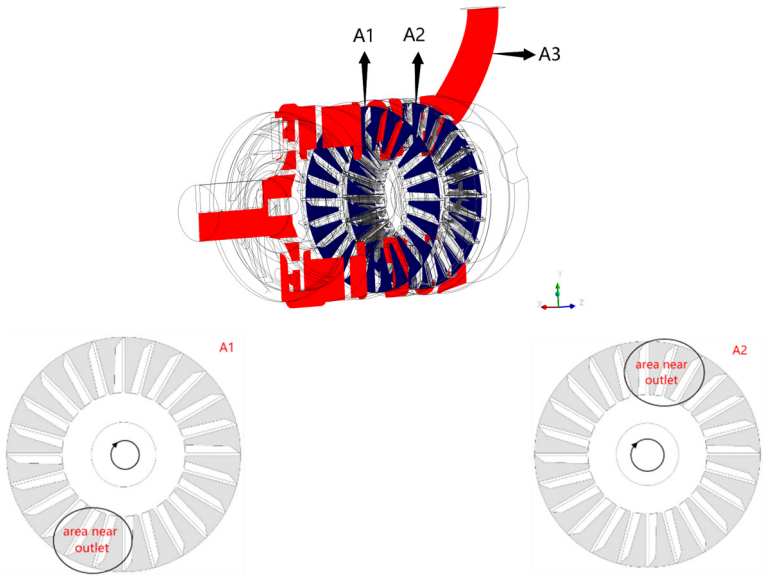

Figure 8. Schematic diagram of simulated sampling physical location.

The pressure and velocity streamline of section A3 are shown in Figure 9. We found that the pressure before and after the two-stage side channel impeller rose significantly. The results showed that the flow exchange in the side channel impeller was the main reason for the increase in pressure. Here, the main function of the front centrifugal impeller was to increase the inlet pressure of the side channel impeller to reduce the occurrence

of cavitation. At the same time, there were obvious vortices in the outlet section and the connecting channel of the centrifugal impeller and the side channel impeller, and the vortex intensity decreased with the increase of flow rate. In the case of a high Reynolds number, the turbulence intensity showed a downward trend. Strong eddy flow currents in the interstage connected flow channel led to flow losses. Thus, the interstage connecting channel could be optimized. The streamlines at the valley of the head were more complex than those at the peak, which was related to the working mode of the side channel pump. This explained, to a certain extent, the reason why it was at the valley point of the head and the efficiency. Again, too much vortex brought a greater flow loss, which led to the decline of the head and the efficiency. By comparing the DES and SST models, we found that the DES model more accurately described the core and flow details of each vortex. This was because the RANS model limited the vortex shedding, resulting in the neglect of small-scale vortices. As a RANS–LES hybrid model, the DES model was able to identify and describe the smaller vortices by using the LES model's subscale vortex separation method, which has an important impact on the analysis of numerical simulations.

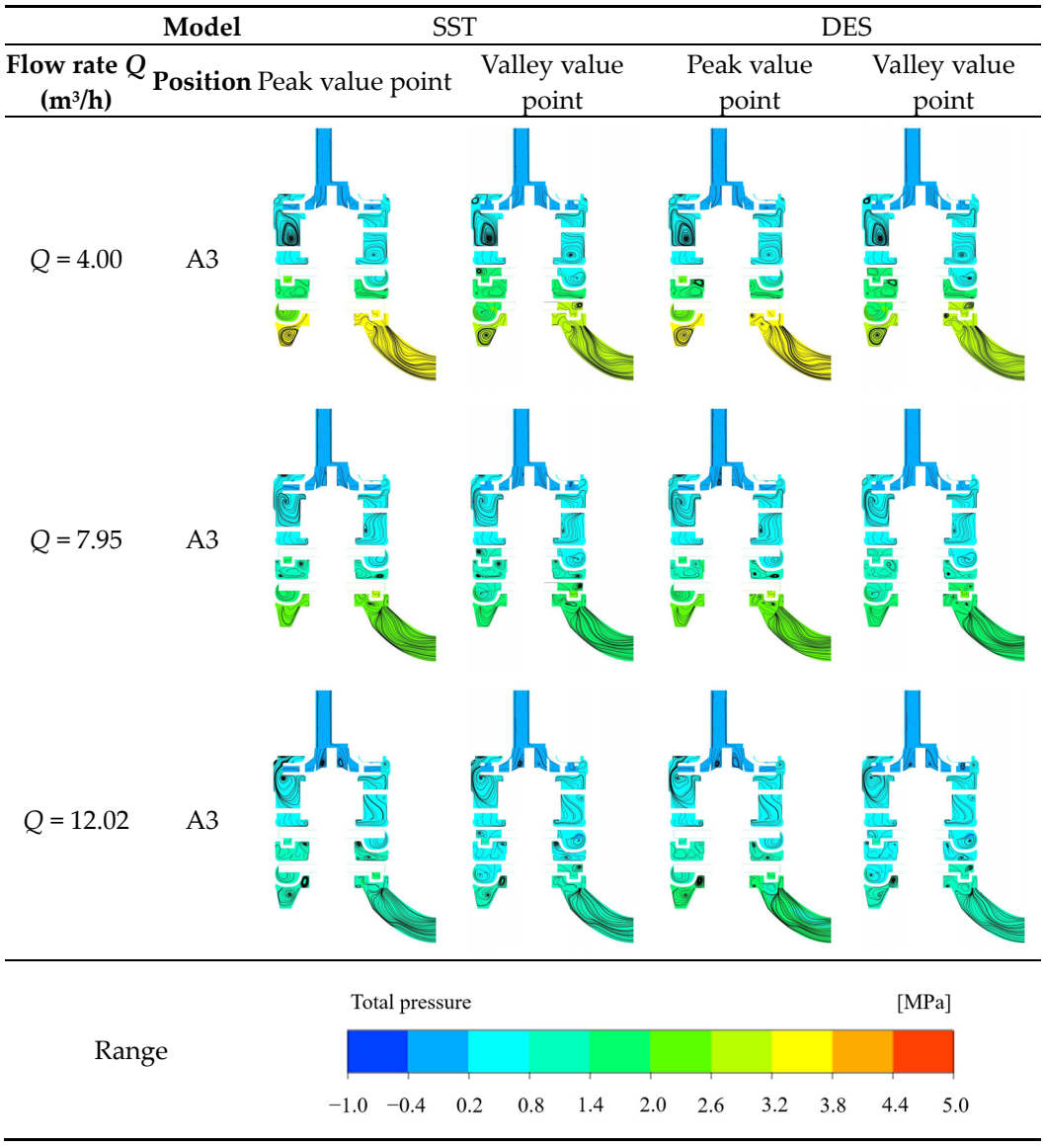

Figure 9. Meridional plane streamlines pressure distribution of the SST and DES models at the peak and valley points of the head.

Figure 10 shows the velocity situation. The velocity streamlined the distributions of the SST and DES models at A1 and A2, near the outlet at the peak and valley point of the head. The following points are shown in Figure 10. First, the vortex phenomenon of the side channel impeller is more obvious in the inlet and outlet area. There was a complex flow exchange in the inlet and outlet regions of the side channel impeller, which led to a large number of unstable turbulences. Second, at the valley point of the head, the vortex in the impeller was more complex than the peak point of the head. This was consistent with the results shown in Figure 9. Third, as was the case on the A3 plane, the vortex became sparse with the increase of flow rate. At a higher flow rate, the inertial force of the fluid increased and the fragmentation of the fluid flow decreased. The large-scale vortex increased and the small-scale vortex decreased. Fourth, the eddy flow currents on the A2 surface and the A1 surface were basically the same, except for the change in the inlet and outlet positions. This corresponded to the flow pattern shown in Figures 11 and 12. The vortices were concentrated in the blade root area (*inner radius*), a large number of the streamlines guided the blade suction surfaces, and the vortices in the inlet and outlet areas were obviously greater. This was in line with the working principle of the side channel impeller. The liquid flow entered the impeller from the blade outer radius and flowed to the side channel from the blade root, which caused the liquid flow to break, due to impact on the blade root, and form a vortex. The flow to the suction surface of the blade also led to the generation of the vortex. Finally, the DES model described more small-scale vortices, because the LES model can separate smaller scale vortices from liquid flow.

Figure 11 provides a view of vortex core area of the two-stage side channel impeller, and Figure 12 shows the volume comparison diagram of the vortex core area. The method of determining the vortex core region uses the Q-criterion, which is the difference between the vorticity and the strain rate. The larger the value, the more obvious the vorticity. This method is widely used in the analysis of vortex treatment because of its small amount of calculation and excellent treatment effect. The formula [24] is as follows:

$$q = -\frac{1}{2}\left[\left(\frac{\partial u_i}{\partial x_i}\right)^2 + \left(\frac{\partial u_j}{\partial x_j}\right)^2 + \left(\frac{\partial u_k}{\partial x_k}\right)^2\right] - \frac{\partial u_i \partial u_j}{\partial x_j \partial x_i} - \frac{\partial u_i \partial u_k}{\partial x_k \partial x_i} - \frac{\partial u_j \partial u_k}{\partial x_k \partial x_j} \quad (23)$$

When the value was $8.82 \times 10^5\ s^{-2}$, a more detailed image could be obtained. It can be seen that the vortex was concentrated near the blade and the blade root. There was a complex vortex structure in the inlet and outlet ports. The following conclusions were drawn, based on the information shown in Figures 11 and 12. The volume of the vortex core areas of the different impellers was very close. This showed that different pressure intensities did not have a significant impact on the generation of eddy flow currents. In addition, the vortex volume at the head valley point was 9.8% larger than that at the head peak point. This showed that different pressures did not have a great impact on the generation of eddy current. In addition, the vortex core volume of the SST model was slightly larger than that of DES model, with an average of 6.24%. This was because the DES model captured small-scale vortices that could not be identified by the RANS model, thereby refining the large vortices that were identified by SST. Figures 10 and 11 show that the vortex and vortex core area displayed by the streamline were highly consistentin the impeller root, the impeller suction surface, and the inlet and outlet areas. This was consistent with the phenomenon expressed in the velocity streamline behavior, as shown in Figure 10. Finally, Figure 11 also indicates that there are vortices on the interface between the side channel and the impeller. They are concentrated at the inlet and outlet areas, because of the complex momentum exchange near the inlet and outlet areas. The corresponding streamline could not be observed in the middle section of the impeller.

Model		SST		DES	
Flow rate Q (m^3/h)	**Position**	Peak value point	Valley value point	Peak value point	Valley value point
Q = 4.00	A1	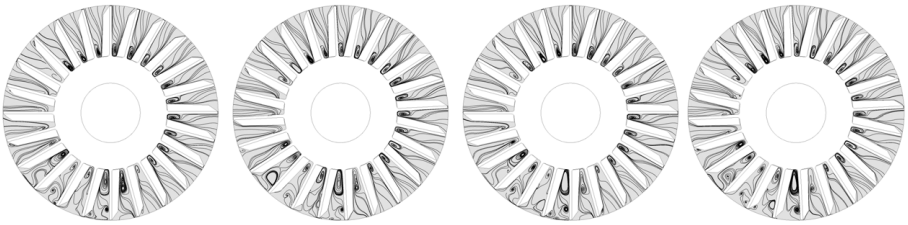			
	A2	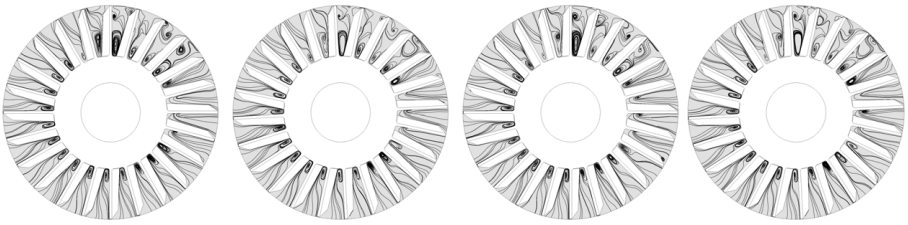			
Q = 7.95	A1	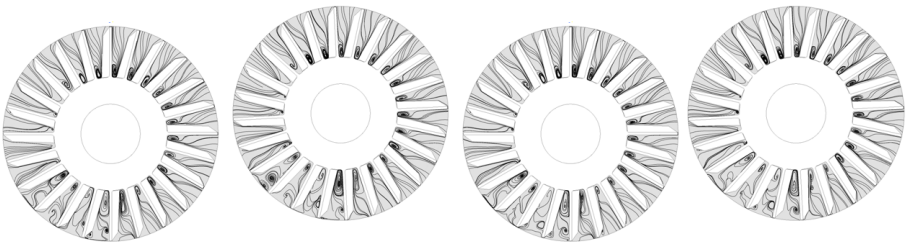			
	A2	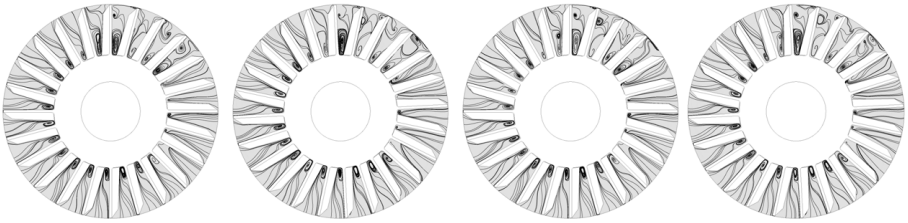			
Q = 12.02	A1	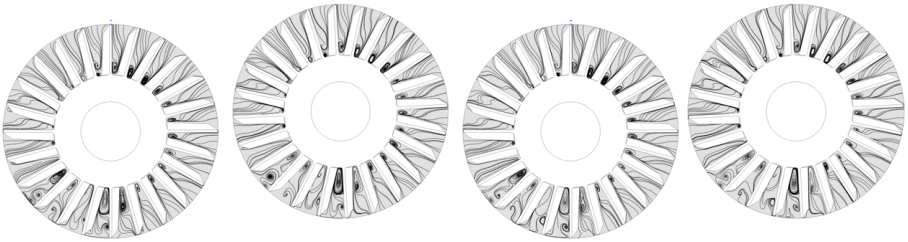			
	A2	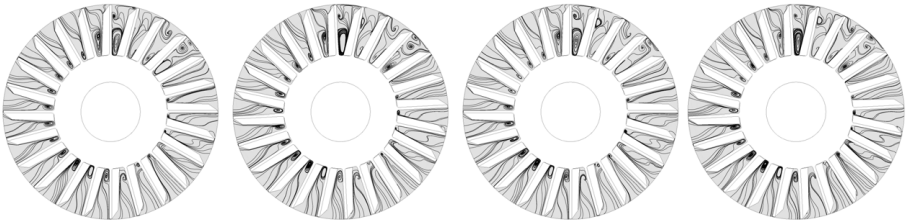			

Figure 10. Velocity streamlines distributions of the SST and DES models at A1 and A2 near the outlet at the peak and valley points of the head.

Model		SST		DES	
Flow rate Q (m3/h)	**Position**	Peak value point	Valley value point	Peak value point	Valley value point
Q = 4.00	First stage side channel impeller				
	Second stage side channel impeller			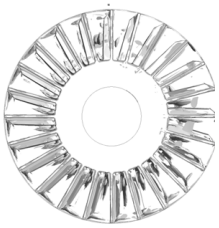	
Q = 7.95	First stage side channel impeller				
	Second stage side channel impeller				
Q = 12.02	First stage side channel impeller				
	Second stage side channel impeller	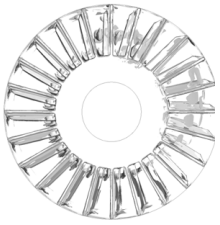	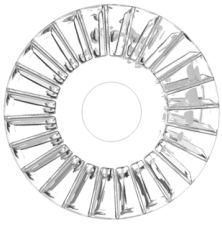		

Figure 11. Distribution of vortex core area of side channel impeller with the SST and DES models at the peak and valley points of the head (instantaneous).

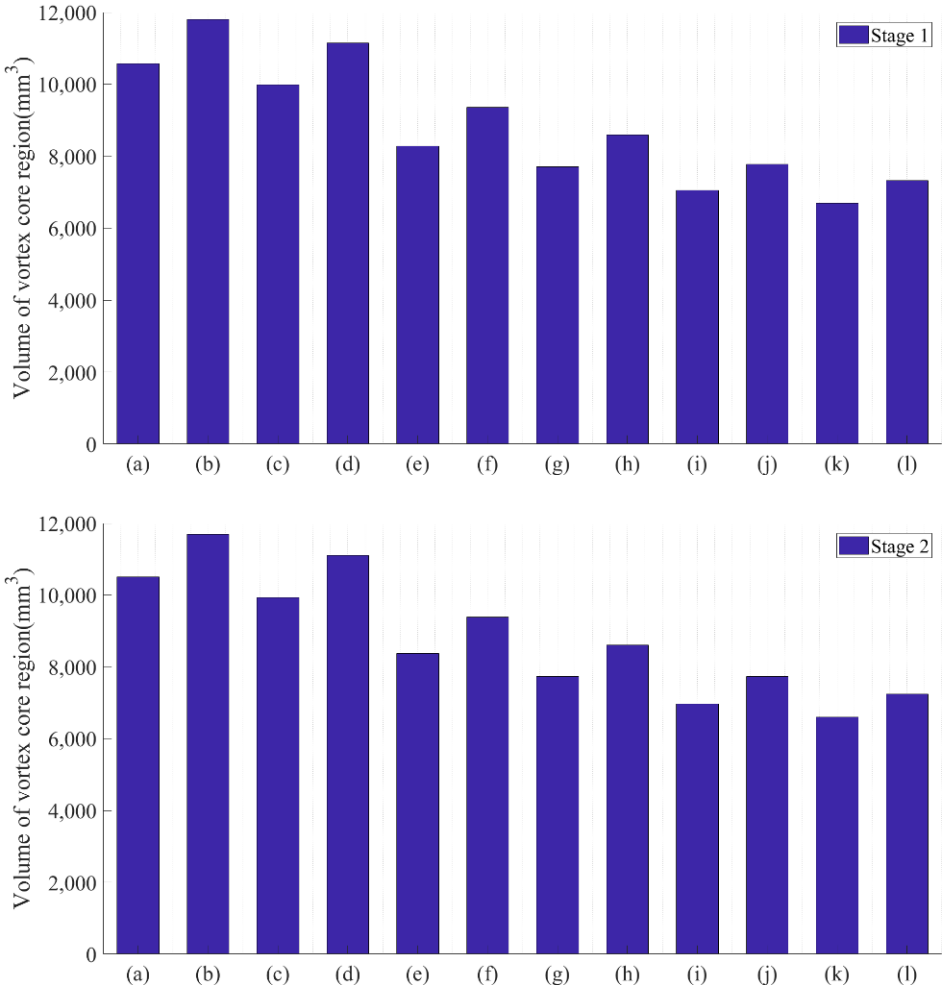

Figure 12. Volume comparison of vortex core area (instantaneous) of different side channel impellers at the same stage with the SST and DES models (a) Q4-SST-P, (b) Q4-SST-V, (c) Q4-DES-P, (d) Q4-DES-V, (e) Q8-SST-P, (f) Q8-SST-V, (g) Q8-DES-P, (h) Q8-DES-V, (i) Q12-SST-P, (j) Q12-SST-V, (k) Q12-DES-P, and (l) Q12-DES-V.

According to the above comparison and discussion, the output results of the SST model and the DES model are basically consistent in hydraulic performance. They reflect the working characteristics and the internal flow law of multistage side channel pumps to a certain extent. However, the DES model, which can identify smaller eddy currents, is superior to the SST model in eddy current identification. This is very important for the side channel pump, the work mode of which is directly related to eddy current. Therefore, in the next stage, follow-up research will be carried out, based on the DES model.

4.2. Effects of the Curvature Correction Model

The flow in the side channel pump, as a type of vortex pump, enters the impeller outer radius and returns from the side channel to the blade's inner radius. Because of this, there is a large amount of mass momentum exchange between the static domain of the side channel and the rotating domain of the impeller in a single cycle. When the impeller speed of the model pump was high, curvature correction had a great influence on the numerical simulation results of the side channel pump.

Table 4 and Figure 13 show the simulation results of hydraulic performance based on the DES model, with or without curvature correction, at different flow points. We found that after curvature correction, the hydraulic performance was relatively closer to the experimental data, and the accuracy of the simulation results had significantly improved.

The changing trend of the head and the efficiency at different flow points conformed to the experimental data, which reflected the working law of the multistage side channel pump. This information be used to provide an analysis sample of the internal flow law of the multistage side channel pump.

Table 4. The hydraulic performance simulation results based on the DES model, with and without curvature correction, and the hydraulic performance experimental results at different flow points.

Flow Rate Q (m^3/h)	Turbulence Model	Head/(m)	Efficiency/(%)
Q = 4.00	No curvature correction	314.35	15.727
	Curvature correction	306.01	15.538
	Experiment	271.84	15.700
Q = 7.95	No curvature correction	211.30	28.440
	Curvature correction	205.59	27.871
	Experiment	182.10	27.900
Q = 12.02	No curvature correction	108.57	31.918
	Curvature correction	102.37	30.960
	Experiment	90.39	31.300

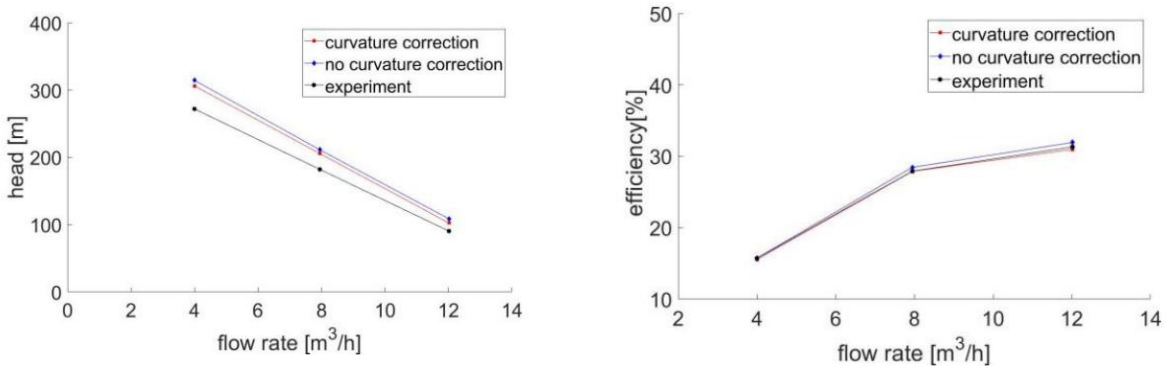

Figure 13. The hydraulic performance simulation results based on the DES model, with and without curvature correction, and the hydraulic performance experimental results at different flow points.

Figure 14 shows the meridional plane streamlines and pressure distribution, with or without curvature correction. After curvature correction, the streamlines became smoother. This was because, after curvature correction, the role of the rotation effect was reflected, which delayed the separation of the boundary layer [25] and reduced the flow loss caused by turbulence. We also found that the overall vortex intensity decreased. The streamline in the side runner was clearer. In addition, the law of pressure distribution was completely consistent with that of Figure 9.

The conclusion illustrated in Figure 15 is similar to that shown in Figure 10. We found that after curvature correction, the vortex was farther away from the blade surface. On different impellers, curvature correction also had some effects on the pressure distribution. The secondary flow caused by the rotation effect stabilized the boundary layer on the convex surface and destabilized the boundary layer on the concave surface [25]. This made the flow channel in the side channel impeller more stable but brought more vortex to the side channel. The vortices were concentrated near the inner and outer radii of the blade. After curvature correction, the volume of the vortices was reduced but the intensity of the vortices was increased, and the vortices became easier to identify.

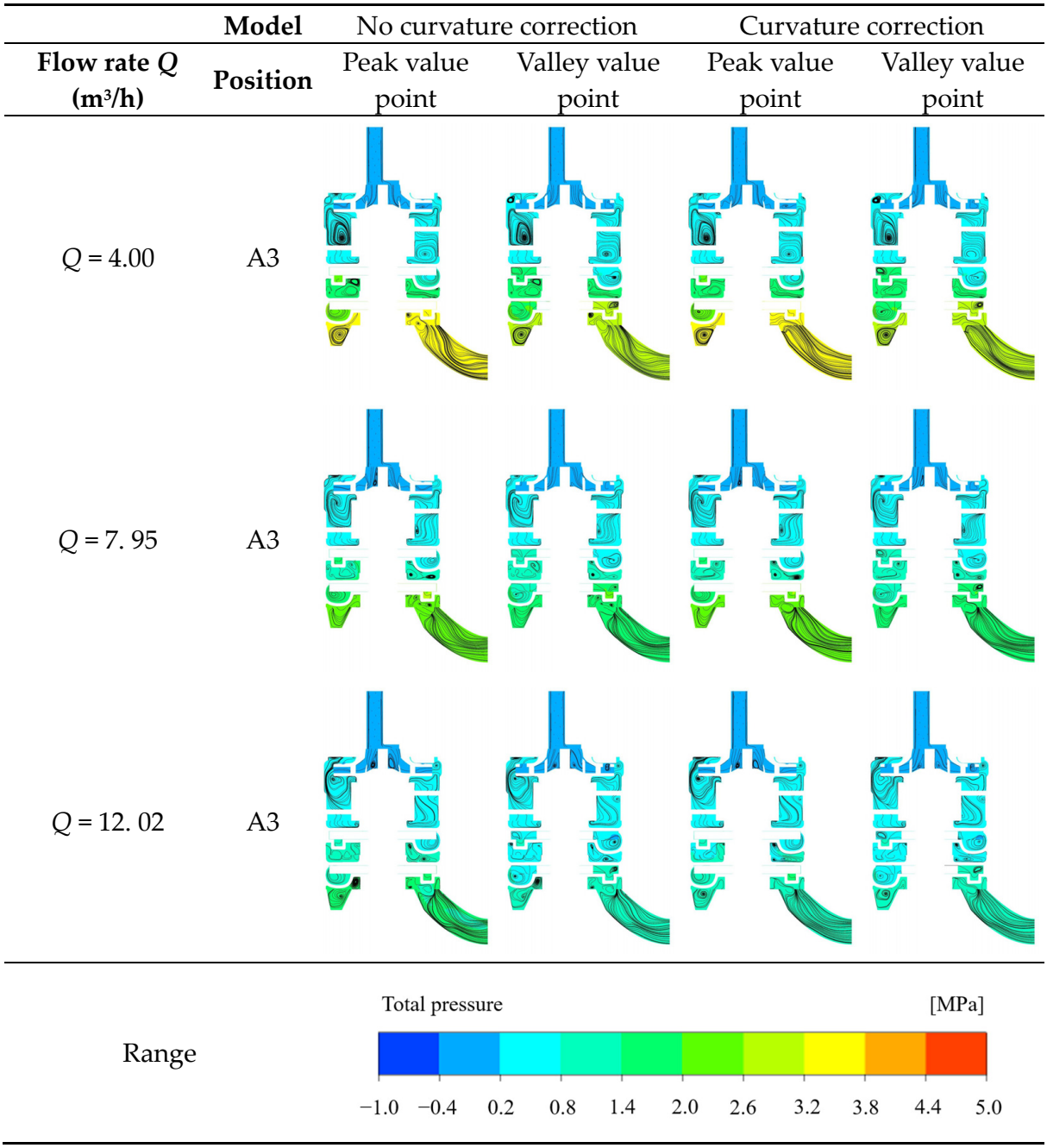

Figure 14. Meridional plane streamlines pressure distribution based on the DES model, with or without curvature correction at the peak and valley points of the head.

Figures 16 and 17 provide the following information. First, the vortex was concentrated in the blade root and blade suction surface area, and an obvious vortex also appeared in the inlet and outlet areas, which was consistent with the situation described in the streamline diagram. When the head was at the valley point, the vortex became sparse. This was consistent with the flow patterns mentioned in the previous section. There was no obvious difference in the vortex distribution of the two-stage side channel impeller, except for the difference caused by the inlet and outlet positions. This situation occurred because the working conditions of the two-stage side channel pump are relatively independent and the difference in inlet liquid flow is small. Finally, after curvature correction, the volume of the vortex core in the impeller area decreased significantly. This phenomenon was consistent with the conclusion that the secondary flow caused by the rotation effect could promote

the stability of the convex boundary. Via this analysis, we found that the rotation effect of side channel pump, as a type of vortex pump, had a great influence on its description of vortex. This reduced the eddy current in the impeller area and caused the boundary layer in the other areas to fall off faster, resulting in the drop of the head and the efficiency of the overall numerical simulation, which was more in line with the actual situation. As part of the study of side channel pumps, the analysis of the vortex is very important.

Model		No curvature correction		Curvature correction	
Flow rate Q (m³/h)	**Position**	Peak value point	Valley value point	Peak value point	Valley value point
Q = 4.00	A1	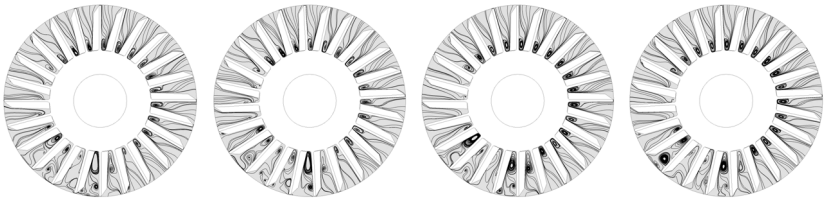			
	A2	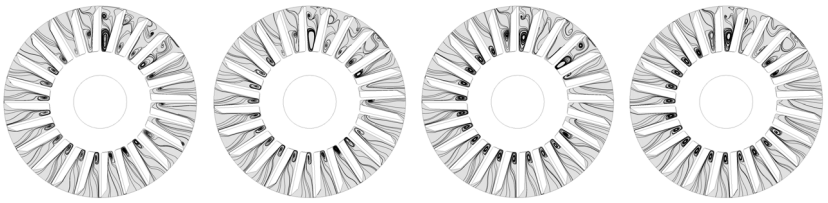			
Q = 7.95	A1	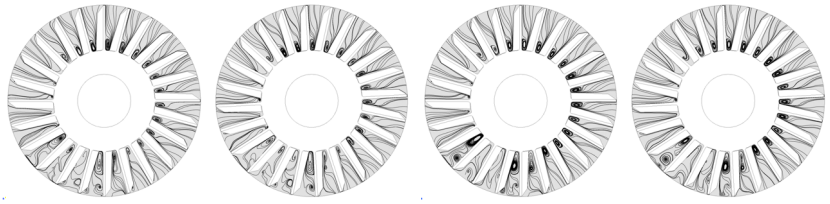			
	A2	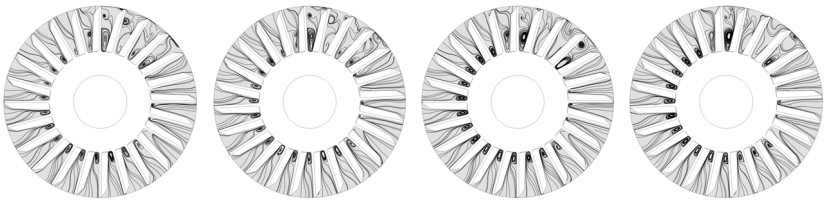			
Q = 12.02	A1	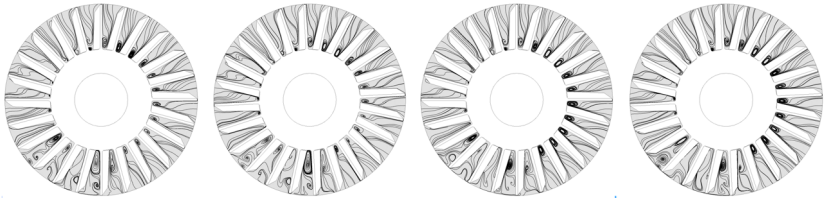			
	A2	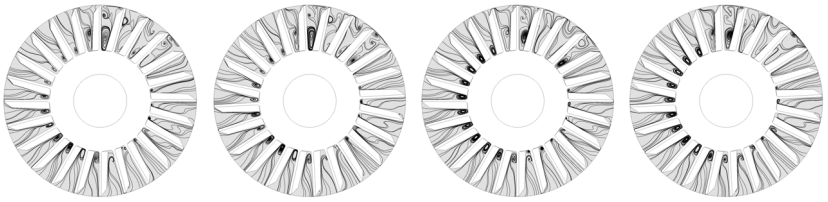			

Figure 15. Streamline distribution based on the DES model, with or without curvature correction at A1 and A2 near the outlet at the peak and valley points of the head.

	Model	No curvature correction		Curvature correction	
Flow rate *Q* (m³/h)	**Position**	Peak value point	Valley value point	Peak value point	Valley value point
Q = 4.00	First stage side channel impeller	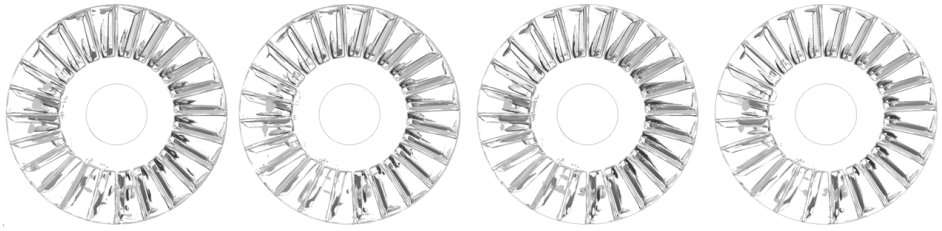			
	Second stage side channel impeller	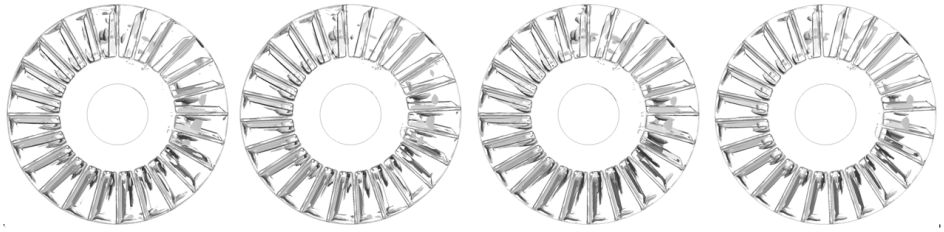			
Q = 7.95	First stage side channel impeller	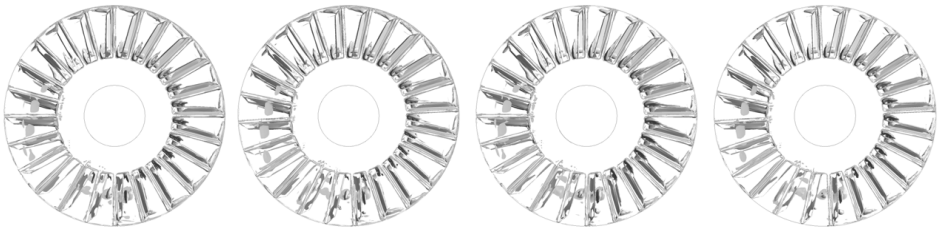			
	Second stage side channel impeller	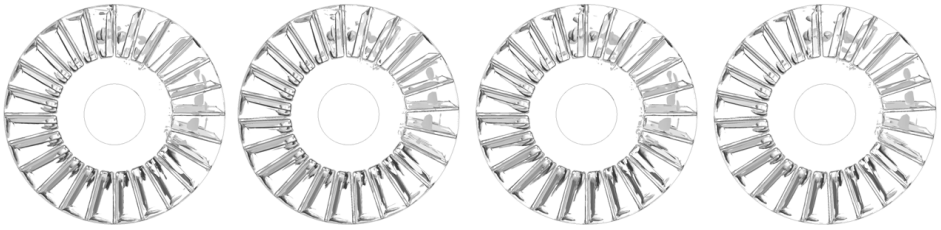			
Q = 12.02	First stage side channel impeller	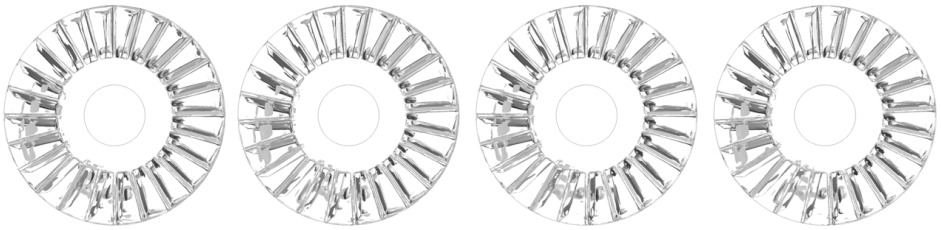			
	Second stage side channel impeller	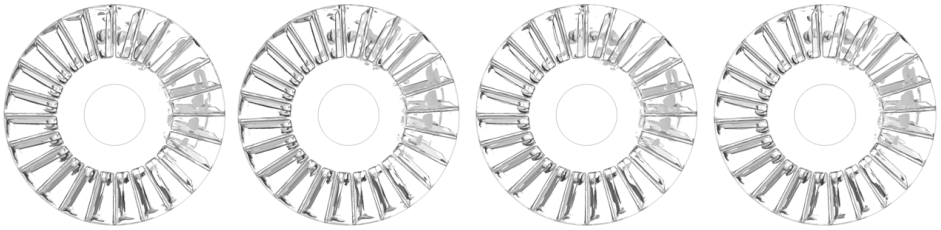			

Figure 16. Distribution of vortex core area of side channel impeller based on the DES model, with or without curvature correction at the peak and valley points of the head (instantaneous).

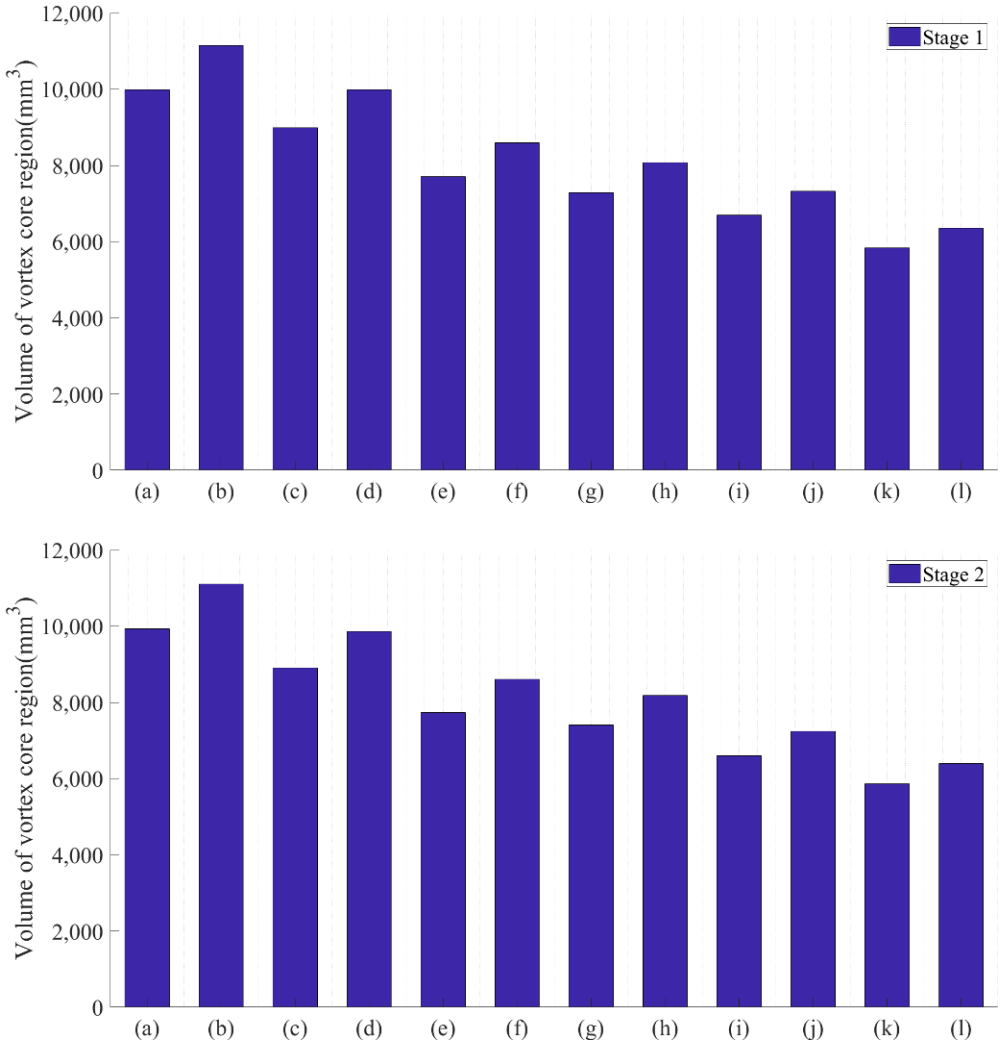

Figure 17. Volume comparison of vortex core area (instantaneous) of different side channel impellers at the same stage based on the DES model with or without curvature correction (a) Q4-NCC-P, (b) Q4-NCC-V, (c) Q4-CC-P, (d) Q4-CC-V, (e) Q8-NCC-P, (f) Q8-NCC-V, (g) Q8-CC-P, (h) Q8-CC-V, (i) Q12-NCC-P, (j) Q12-NCC-V, (k) Q12-CC-P, and (l) Q12-CC-V.

Because the main pressurization area is located in the side channel impeller, the turbulent kinetic energy distribution inside the side channel impeller was analyzed, and its distribution diagram is shown in Figure 18. It can be seen that the turbulent kinetic energy was higher on the blade root and the blade pressure surface. In addition, although it was not as high as the turbulent kinetic energy of the blade pressure surface, the turbulent kinetic energy of the blade suction was also slightly higher than the gap between the blades. This was consistent with the law shown in the streamline and vortex distribution diagram. The liquid flow was broken on the blade root and the blade pressure surface, forming more vortices and bringing higher turbulent kinetic energy. The turbulent kinetic energy was not high near the inlet and outlet. This was because, in the inlet and outlet area, the vortex was more concentrated in the junction area between the impeller and the side channel, as verified in Figures 16 and 17. At the same time, without considering the secondary flow caused by the rotation effect, it was difficult to estimate the turbulent kinetic energy distribution near the blade pressure surface in the DES model, resulting in its inaccurate description of some vortices. In addition, with the increase in flow rate, the inertial force of the liquid flow increased, the eddy current intensity decreased, and the turbulent kinetic energy also decreased. At a high Reynolds number, the eddy current

intensity decreased with the increase in the Reynolds number, resulting in the decrease of turbulent kinetic energy. These results show that curvature correction has an important influence on numerical simulation, not only in the description of the eddy flow current but also in the distribution and loss of turbulent kinetic energy.

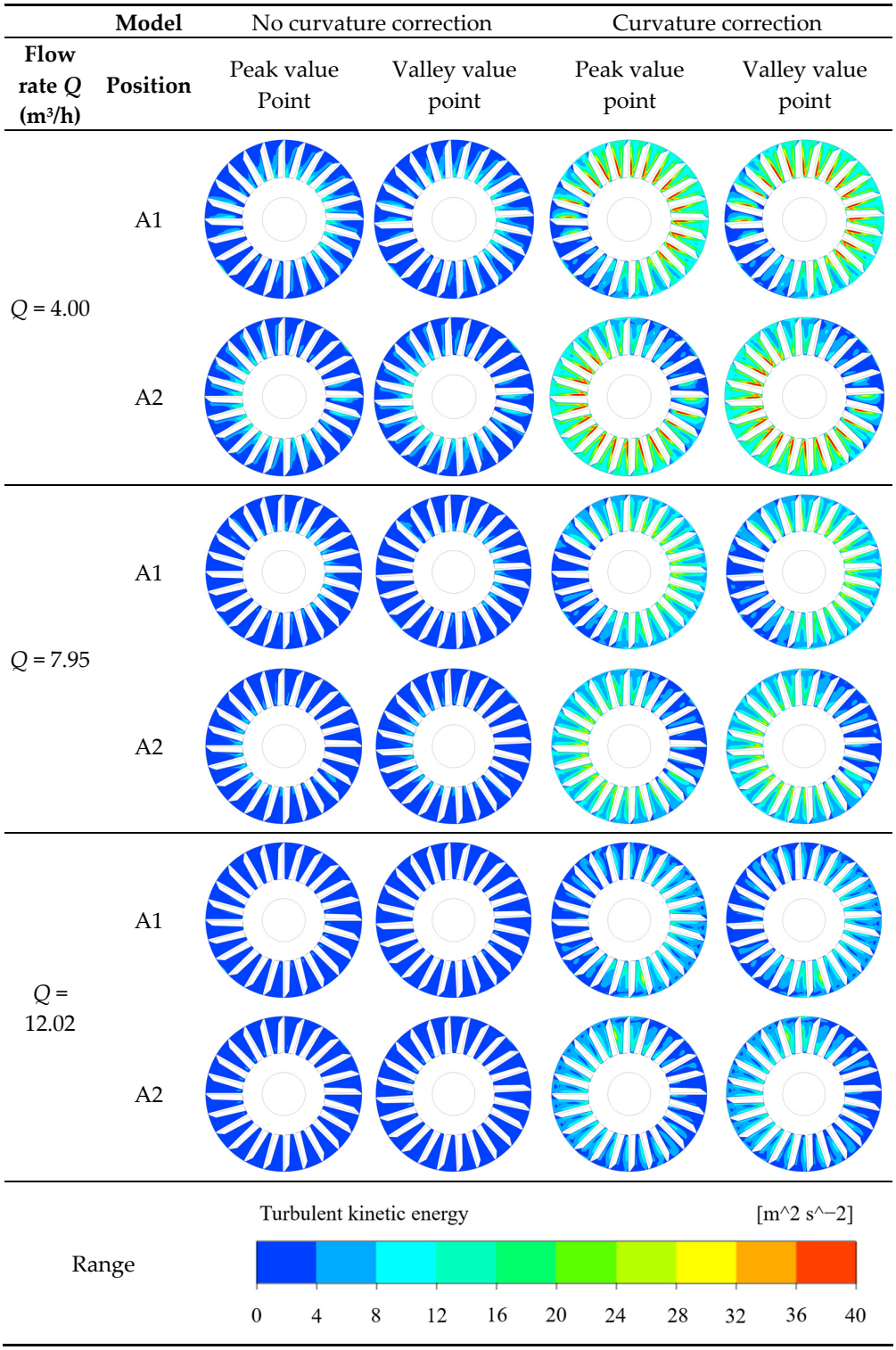

Figure 18. Turbulent kinetic energy distribution based on the DES model with or without curvature correction at A1 and A2, at the peak value point and the valley value point of the head.

Curvature correction is very important for the numerical simulation of multistage side channel pump. Whether in vortex analysis, streamline analysis, or turbulent kinetic energy analysis, curvature correction can greatly improve the numerical model of multistage side channel pumps and, to a certain extent, affect the numerical simulation of hydraulic performance making the simulation more suitable for the actual situation. Therefore, curvature correction is an important parameter that must be taken into account in the numerical simulation of a high-speed rotating domain with a large amount of mass and energy exchange between the rotating domain and the stationary domain.

5. Conclusions

In this study, we first discussed the influence of the RANS model and the hybrid RANS–LES model on the numerical simulation of a multistage side channel pump, and then discussed the influence of curvature correction on the numerical simulation of such a pump. We reached the following conclusions.

(1) From the comparison, we found that the SST model and the DES model were almost the same in hydraulic performance, while the DES model was better in simulating the subscale vortex.
(2) After curvature correction, the hydraulic performance simulation results were improved, the turbulent kinetic energy distribution was more clear, and the energy loss of the multistage side channel pump could be better analyzed.
(3) For a more detailed comparison, the middle part of the two-stage side channel impeller and the meridional surface of the pump were selected to compare the streamline, turbulent kinetic energy, and vortex. By comparing the SST model with the DES model, we found that the DES model described the subscale vortices in greater detail.
(4) We increased the curvature to correct the decrease of vorticity in the rear channel impeller. At the same time, curvature correction made the description of turbulent kinetic energy more detailed, which was very helpful for subsequent analysis.

Through the above analysis, we concluded that the DES-CC model, compared with other models, can more accurately analyze the multistage side channel pump and better predict its performance. In subsequent work, the influence of other turbulence models on the numerical simulation of multistage side channel pumps can be verified by other advanced measurement methods.

The above conclusions are the simulation results under the three-degree time step. The advantages of the DES model cannot be overstimated. Therefore, the DES-CC model will be simulated, in the future, in a shorter time step to obtain more accurate results.

This study lays the foundation for further study on the cavitation performance, the pressure pulsation, the gas–liquid mixed transport performance, and the timing effect of multistage side channel pumps.

Author Contributions: Conceptualization, R.L. and K.C.; Data curation, R.L.; Formal analysis, R.L.; Investigation, R.L. and K.C.; Methodology, K.C. and Y.W.; Project administration, F.Z., S.Y. and R.X.; Resources, R.L., F.Z., K.C., S.Y. and R.X.; Supervision, F.Z. and S.Y.; Writing—original draft, R.L. All authors have read and agreed to the published version of the manuscript.

Funding: This work was supported by the National Key R&D Program of China (2021YFC3090404), the National Natural Science Foundation of China (Grant No. 52150410397), the Ranking the Top of the List for Science and Technology Projects of Yunnan Province (No.: 202204BW050001), the China Postdoctoral Science Foundation (Grant No. 2021M701535), and the Taizhou Science and Technology Project of China (Grant No. 21gyb05).

Institutional Review Board Statement: Not applicable.

Informed Consent Statement: Not applicable.

Conflicts of Interest: The authors declare no conflict of interest.

Nomenclature

F	blending function
a_1	parameters calculated from turbulence kinetic energy per unit mass and shear stress
C_{DES}	constant (0.61)
k	turbulence kinetic energy per unit mass ($m^2 \cdot s^{-2}$)
L_t	turbulent length scale (m)
P_k	shear production of turbulence ($kg \cdot m^{-1} \cdot s^{-3}$)
Q	flow rate ($m^3 \cdot s^{-1}$)
q	judgment quantity for Q criterion (s^{-2})
S	strain rate (s^{-1})
U_i	velocity ($m \cdot s^{-1}$)
$\overline{U_i}$	average velocity ($m \cdot s^{-1}$)
u_i	wave velocity ($m \cdot s^{-1}$)
y	nearest distance from wall (m)
y^+	nondimensional wall distance
α_1	constant (5/9)
β_1	constant (0.075)
α_2	constant (0.44)
β_2	constant (0.0828)
β'	constant (0.09)
Φ_1	parameter referring to the corresponding coefficient of the $k-\varepsilon$ equation, e.g., α_1, β_1
Φ_2	parameter referring to the corresponding coefficient of the $k-\omega$ equation, e.g., α_2, β_2
Φ_3	parameter referring to the corresponding coefficient of the SST equation, e.g., α_3, β_3
ε	turbulence dissipation rate ($m^2 \cdot s^{-3}$)
ω	turbulence frequency (s^{-1})
ρ	density ($kg \cdot m^{-3}$)
μ	molecular viscosity ($kg \cdot m^{-1} \cdot s^{-1}$)
δ	Kronecker Delta function
μ_t	turbulence viscosity ($kg \cdot m^{-1} \cdot s^{-1}$)
σ_{k1}	turbulence model constant for the k equation (1.176)
σ_{k2}	turbulence model constant for the k equation (1)
$\sigma_{\omega 1}$	turbulence model constant for the k equation (2)
$\sigma_{\omega 2}$	turbulence model constant for the k equation (1/0.856)
Δ	length scale of dissipation rate (m)
τ	shear stress ($kg \cdot m^{-1} \cdot s^{-2}$)
r	parameters calculated from strain rate and curl

References

1. Böhle, M.; Müller, T. Evaluation of the Flow inside a Side Channel Pump by the Application of an Analytical Model and CFD. *Fluids Eng. Div. Summer Meet.* **2009**, *43727*, 11–18.
2. Shirinov, A.; Oberbeck, S. High vacuum side channel pump working against atmosphere. *Vacuum* **2011**, *85*, 1174–1177. [CrossRef]
3. Shirinov, A.; Oberbeck, S. Optimization of the high vacuum side channel pump. In Proceedings of the Seventh International Conference on Compressors and Their Systems, London, UK, 5–6 September 2011; pp. 81–92.
4. Shirinov, A.; Oberbeck, S. Optimisation of the high vacuum side channel pump. In *Research and Development Backing Pumps*; Pfeiffer Vacuum GmbH: Aßlar, Germany, 2011.
5. Fleder, A.; Böhle, M. A systematical study of the influence of blade number on the performance of a side channel pump. *ASME J. Fluids Eng.* **2019**, *141*, 111109. [CrossRef]
6. Fleder, A.; Böhle, M. A systematical study of the influence of blade length, blade width, and side channel height on the performance of a side channel pump. *ASME J. Fluids Eng.* **2015**, *137*, 121102. [CrossRef]
7. Appiah, D.; Zhang, F.; Yuan, S.Q.; Osman, M.K. Effects of the geometrical conditions on the performance of a side channel pump: A review. *Int. J. Energy Res.* **2018**, *42*, 416–428. [CrossRef]
8. Zhang, F.; Appiah, D.; Zhang, J.F.; Yuan, S.Q.; Osman, M.K.; Chen, K. Transient flow characterization in energy conversion of a side channel pump under different blade suction angles. *Energy* **2018**, *161*, 635–648. [CrossRef]
9. Zhang, F.; Appiah, D.; Hong, F.; Zhang, J.; Yuan, S.Q.; Adu-Poku, K.A.; Wei, X. Energy loss evaluation in a side channel pump under different wrapping angles using entropy production method. *Int. Commun. Heat Mass Transf.* **2020**, *113*, 104526. [CrossRef]
10. Zhang, F.; Chen, K.; Appiah, D.; Hu, B.; Yuan, S.; Asomani, S.N. Numerical delineation of 3D unsteady flow fields in side channel pumps for engineering processes. *Energies* **2019**, *12*, 1287. [CrossRef]

11. Zhang, F.; Wei, X.; Chen, K.; Yuan, S.; Wang, Y.; Chen, H. Internal vortex characteristics of side channel pump with convex blade. *J. Agric. Mach.* **2020**, *51*, 115–122.
12. Zhang, F.; Chen, K.; Appiah, D.; Yuan, S.; Adu-Poku, K.A.; Hong, F. Description of unsteady flow characteristics in a side channel pump with a convex blade. *ASME J. Fluids Eng.* **2021**, *143*, 041201. [CrossRef]
13. Mihalić, T.; Guzović, Z.; Predin, A. Performances and flow analysis in the centrifugal vortex pump. *ASME J. Fluids Eng.* **2013**, *135*, 011107. [CrossRef]
14. Yuan, S.Q.; Huang, X.; Zhang, J.F.; Zhang, X. Effects of blade outlet angle on performance of chemical centrifugal pump. *J. Drain. Irrig. Mach. Eng.* **2019**, *37*, 185–191.
15. Kolesov, E.V.; Nakaryakov, E.V. Selection of turbulence model in ventilation modeling for blind stopes. *Earth Environ. Sci.* **2019**, *773*, 012071. [CrossRef]
16. Menter, F.R.; Kuntz, M.; Langtry, R. Ten years of industrial experience with the SST turbulence model turbulence. *Heat Mass Transf.* **2003**, *4*, 625–632.
17. Smagorinsky, J. General circulation experiments with the primitive equations. *Month Weath. Rev.* **1963**, *93*, 99–165. [CrossRef]
18. Strelets, M. Detached eddy simulation of massively separated flows. In Proceedings of the 39th Aerospace Sciences Meeting and Exhibit, Reno, NV, USA, 8–11 January 2001. Paper, 2001-0879.
19. Menter, F.R. Two-equation eddy-viscosity turbulence models for engineering applications. *AIAA J.* **1994**, *32*, 1598–1605. [CrossRef]
20. Germano, M.; Piomelli, U.; Moin, P.; Cabot, W.H. A dynamic subgrid-scale eddy viscosity model. *Phys. Fluids* **1991**, *3*, 1760–1765. [CrossRef]
21. Dong, S.K.; Chung, M.K. Curvature corrections to reynolds stress model for computation of turbulent recirculating flows. *AIAA J.* **1992**, *30*, 2968–2970. [CrossRef]
22. Spalart, P.R.; Shur, M. On the sensitization of turbulence models to rotation and curvature. *Aerosp. Sci. Tech.* **1997**, *1*, 297–302. [CrossRef]
23. Wang, Y.; Zhang, F.; Yuan, S.; Chen, K.; Wei, X.; Appiah, D. Effect of URANS and hybrid RANS-large eddy simulation turbulence models on unsteady turbulent flows inside a side channel pump. *ASME J. Fluids Eng.* **2020**, *142*, 061503. [CrossRef]
24. Zhang, Y.; Zuo, Z.; Liu, J.; Yang, Z. Investigation on small rotary engine in-cylinder turbulent flow based on large eddy simulation. *J. Eng. Thermophys.* **2019**, *40*, 2678–2686.
25. Zhu, B. Prediction of the effects of surface curvature and rotation on the turbulent boundary layers on the centrifugal impellers. *Acta Mech. Sin.* **1987**, *19*, 401–407.